Empirical Determination of Solar Proton Access to the Atmosphere: Impact on Polar Flight Paths

Jason J. Neal and Craig J. Rodger

Department of Physics, University of Otago, Dunedin, New Zealand

Janet C. Green

National Geophysical Data Center, NOAA, Boulder, Colorado

Abstract. Violent expulsions on the Sun's surface release high energy solar protons that ultimately affect HF communication used by aircraft. The geomagnetic field screens the low altitude equatorial region, but these protons can access the atmosphere over the poles. The latitudes over which the solar protons can reach vary with geomagnetic indices such as Kp and Dst. In this study we use observations from Low Earth Orbit to determine the atmospheric access of solar protons and hence the flights paths most likely to be affected. Observations taken by up to six polar orbiting satellites during 15 solar proton events are analyzed. From this we determine 16,850 proton rigidity cutoff estimates across 3 energy channels. Empirical fits are undertaken to estimate the most likely behavior of the cutoff dependence with geomagnetic activity. The changing Kp value is found to lead the variation in the cutoffs by ~3 hours. We provide simple equations by which the geomagnetic latitude at which the protons impact the atmosphere can be determined from a given Kp or Dst value. The variation found in the cutoff with Kp is similar to that used in existing operational models, although we suggest a ~1-2º equatorward shift in latitude would provide greater accuracy. We find that a Kp predictive model can provide additional warning to the variation in proton cutoffs. Hence a prediction of the cutoff latitudes can be made ~3 hours to as much as 7 hours into the future, meeting suggested minimum planning times required by the aviation industry.

1. Introduction

Processes near the Sun can accelerate protons to relativistic energies, producing Solar Proton Events (SPE), also known as Solar Energetic Particle (SEP) events. These protons may make their way to Earth and can cause an operational hazard to aircraft in flight in the polar regions. Here we investigate the access of solar protons to the polar atmosphere and undertake empirical fitting of the observations by which one can predict the regions most likely to be affected. Previous studies have characterized some common features of SPE's. The high-energy component of SPE's is at relativistic levels such that they can reach the Earth within minutes of solar X-rays produced during any solar flares which may be associated with the acceleration. Satellite data show that the protons involved have an energy range spanning 1 to 500 MeV, occur relatively infrequently, and show high variability in their intensity and duration [*Shea and Smart*, 1990]. For large events the duration is typically several days, with risetimes of ~1 hour, and a slow decay to normal flux values thereafter [*Reeves et al.*, 1992].

SPEs are major, though infrequent, space weather phenomena that can produce hazardous effects in the near-Earth space environment. The occurrence of SPE during solar minimum years is very low, while in active Sun years, especially during the falling and rising phases of the solar cycle, SPEs may average one per month. The impacts of SPEs include 'upsets' experienced by Earth-orbiting satellites [*Vampola et al.*, 1994], increased radiation exposure levels for humans onboard spacecraft [*Dayeh et al.*, 2010] and high-altitude aircraft [*Matthiä et al.*, 2009; *Mertens et al.*, 2010], the production of NOx [*López-Puertas et al.*, 2005] and HOx [*Verronen et al.*, 2006] in the middle atmosphere which have been experimentally observed leading to polar mesospheric ozone depletions [*Seppälä et al.*, 2006], strong increases in D-region ionization [*Rodger et al.*, 2006] and upper stratospheric conductivity [*Kokorowski et al.*, 2012], as well as disruption to VLF through to HF/VHF communications in mid- and high-latitude regions [*Davies*, 1990; *Clilverd et al.*, 2005].

In studies into the atmospheric and climatic effects of SPE it is common to assume that the protons impact the polar atmosphere using a simple cutoff, for example poleward of a geographic latitude of 60° [e.g., *Jackman et al.*, 2009]. However, in reality access to the atmosphere is determined by the partial guiding of the geomagnetic field. The first description of cosmic rays in the Earth's magnetic field [*Störmer*, 1930] demonstrated the geomagnetic cutoff rigidity, the minimum rigidity a particle must possess to penetrate to a given geomagnetic latitude and altitude, where the rigidity of a particle is defined as the momentum per unit charge. Therefore, every geomagnetic position has a corresponding cutoff rigidity. Higher rigidities are required to reach lower geomagnetic latitudes, and thus all particles with rigidities larger than the minimum can penetrate to that latitude and altitude (and all higher latitudes). *Cooke et al.* [1991] provide a considerably more detailed description of geomagnetic cutoff rigidities.

Multiple approaches have been used to determine the geomagnetic cutoff and to consider how this varies with geomagnetic activity. For example, *Leske et al.* [2001] used observations from the low-Earth orbiting satellite SAMPEX to measure the location of the geomagnetic cutoff during several large solar energetic particle events from 1992-1998, and showed the variation in the cutoffs tracked well with the variations in the Kp and Dst geomagnetic indices. These observations found that the cutoff latitude could vary quite rapidly, often by more than 5º in less than one day. A different approach has been to trace particles through models of the Earth's field producing grids of estimated cutoff rigidities distributed over the Earth at a given altitude [e.g., *Smart and Shea*, 1985; *Smart et al.*, 2003; *Kress et al.*, 2010], and SAMPEX data has been used to test the quality of these models [see the discussion in *Kress et al.*, 2010]. Satellite observations have the advantage of making global comparisons, but suffer from relatively low time resolution; in a ~90 min SAMPEX orbit the spacecraft will cross the polar regions 4 times. Ground-based observations have also been used to test the field-traced cutoffs models, with the advantage of much higher time resolution (~1 min) but limited spatial coverage. One ground-based approach used a combination of imaging riometer observations from Antarctica and ionospheric modeling during solar proton events where the rigidity cutoff swept back and forth across the instrument's field of view during six different SPE periods [*Rodger et al.*, 2006; *Clilverd et al.*, 2007]. The ground-based studies found the particle-tracing cutoffs determined by *Smart and Shea* [2003] using an extended Tsyganenko-1989 geomagnetic field model was accurate up to Kp≈5, but produced cutoff latitudes for larger geomagnetic storms that were too far equatorwards. In this study we will use a very large database of low-Earth orbit satellite observations to more accurately describe the cutoff latitudes and how they vary with geomagnetic activity.

As solar proton events lead to large increases in D-region ionization densities, they produce large increases in ionospheric attenuation, termed Polar Cap Absorption (PCA). The ionospheric effects of SPEs were first identified through the large absorption increases in VHF communication links during the 23 February 1956 event [*Bailey*, 1957]. This affect is particularly pronounced for radio waves in the HF range; SPE-produced PCA can lead to complete blackouts of HF communications through the polar regions lasting several days. For HF radio waves the primary contributors to PCA are protons with energies near 20 MeV [*Patterson et al.*, 2001] with the threshold energy being >10 MeV [*Kavanagh et al.*, 2004] for day and >5 MeV for night [*Clilverd et al.*, 2007]. HF radio communications blackouts are of importance to commercial aviation using polar flight routes. For example, it is a US Federal regulation commonly followed by all international airlines that flights must maintain communications with Air Traffic Control and their company over the entire route of flight. Many airlines rely on SATCOM, Satellite Communications with geostationary satellites. Unfortunately above 82° latitude they are unable to use SATCOM, due to lack of satellite transmission access (line of sight) [*Sauer and Wilkinson*, 2008]. Thus for latitudes above 82°, HF radio is used for aircraft communication which is susceptible to PCA during solar proton events. For safety when SPEs occur, aircraft travelling on polar routes need to be diverted to latitudes below 82°, to keep line of sight with the satellites, and be able to communicate via SATCOM [*National Research Council*, 2008]. A schematic of this is shown in Figure 1, where PCA disrupts HF communications in the polar regions, but not at mid-latitude. Airlines who do not use SATCOM or who want to retain HF communications as a backup would need to avoid large parts of the polar regions, due to the impact of PCA; this will also apply to ground-based installations including HF receivers at some airports.

Cross polar flights are growing in number with 10,993 flights in 2011 [*Albersheim and Gunzelman*, 2012], up from 7,300 polar flights in 2007 [*National Research Council*, 2008]. These routes are favored as they are more direct, leading to shorter flight times and thus smaller fuel burn. An example of polar routes are shown in Figure 2; note that significantly more polar routes occur in the northern hemisphere than the southern due to the distribution of land. There are a significant number of dedicated cross polar routes above 82°N which are particularly used for the regular commercial flights from eastern North America to Asia [*National Research Council*, Figure 5.1, 2008].

Even with the availability with SATCOM, airline operations are still disrupted by SPE. In practice airlines change their flight paths during large SPE, and air traffic control modifies its operation. In January 2005 United Airlines diverted 26 flights to non-polar or less-than-optimum polar routes for several days to avoid the risk of HF radio blackouts during PCA events [*National Research Council*, 2008]. Similarly, in January 2012 Delta Airlines rerouted some transpolar flights between Asia and the U.S. to avoid the impact of the largest SPE which had occurred in almost a decade [*Cameron*, 2012], where "largest" refers to the >10 MeV proton flux. In this event 8 Delta airline flights were routed outside the pole entirely due to concerns around HF communications and travelers health, with at least another 8 flights affected in March 2012 due to another large SPE [*Fahey and Scott*, 2012]. Polar Air Traffic controllers also reported significant communications difficulties in the January and March 2012 events. The FAA provided the following report: "limited reliable

HF communications forced aircraft operators to use other communication methods", but despite the availability of SATCOM in the latitudes of the flights paths "at times, communications were impossible" [*Federal Aviation Administration*, 2012]. In the March 2012 SPE aircraft operators moved their flight paths from above 80°N to those around 70-72°N, leading to congestion on these paths. The SPE-produced HF communication disruptions caused the air traffic control centers to increase the separation of the aircraft from 10 min to 15 min.

In this paper we exploit the large number of POES satellites in low-Earth orbit to empirically determine the geomagnetic cutoff latitudes which determine the access of solar protons to the polar atmosphere. With as many of six POES-satellites, this comparison allows global coverage and 24 cutoff measurements across the ~100 min orbital period, leading to time resolution close to that from ground-based instruments. We particularly focus on those protons which will affect the D-region to produce Polar Cap Absorption, and hence degrade HF communications in the polar regions. As Polar Cap Absorption events can influence the choice of flight paths used by commercial aviation, thereby increasing fuel-burn and thus cost, our goal is to produce a simple experimentally based predictor of the likely polar zone in which Polar Cap Absorption events will occur linked to varying geomagnetic activity levels. Such expressions should also be useful to those researchers who want to investigate SPE effects in atmospheric chemistry and dynamics, allowing a more realistic description of the particle impact on the polar atmosphere. This provides a test, and a data-driven refinement, of the Smart and Shea modeling which are currently used in operational models.

2. Instrumentation and data

2.1 POES Satellite Data

Here we use data from the second generation Space Environment Monitor (SEM-2) flown on the Polar Orbiting Environmental Satellites (POES) series of satellites, and on the

Meteorological Operational (MetOp)-02 spacecraft. For our study period there are at least three and often six satellites that carry the SEM-2 instrument package, depending on the time of the SPE. The spacecraft are in Sun-synchronous polar orbits with typical parameters of ~800−850 km altitude, 102 min orbital period and 98.7° inclination [*Robel*, 2009]. The orbits typically are either morning or afternoon equator crossings, with corresponding night-time crossings. Table 1 contains a summary of the SEM-2 carrying spacecraft operational at the time of writing.

The SEM-2 package includes the Medium Energy Proton and Electron Detector (MEPED) which was designed to monitor the intensities of protons and electrons over a range extending from 30 keV to greater than 200 MeV [*Evans and Greer*, 2004]. We focus on observations from the four omnidirectional dome detectors which are ±60° wide and are mounted so that their centre of view is looking outwards along the local zenith, parallel to the Earth-centre-to-satellite radial direction. The proton flux difference between each of the four omnidirectional channels was taken. This gave three finite and narrower integral passband ranges, i.e. the difference between the omnidirectional P6 and P7 fluxes gives fluxes in the 16-35 MeV range. To assign each of these to a single specific energy value the logarithmic average was taken for each passband, as given in Table 2. Note that this assumes that the fluxes reported from each dome detector can be directly compared.

We make use of the raw 2-s resolution binary files which had been downloaded from http://satdat.ngdc.noaa.gov/sem/poes/data/full/. All parameters were interpolated down to a consistent 2-s time resolution. The accumulation period for two of the omnidirectional telescopes is 2-s (P6 and P7), while the other two have a 4-s accumulation periods (P8 and P9) and the orbital parameters for the spacecraft have 8-s resolution. The orbital information, such as the IGRF *L*-shell parameter, for the satellites had been generated using the IGRF magnetic field model with the prior knowledge of the satellites orbit, using the epoch midway through the year the data were acquired [*Evans and Greer*, 2004]. POES omnidirectional proton data includes a large near-constant flux of protons in the South Atlantic. These protons are a trapped population that is part of the inner Van Allan radiation belt [*Vernov et al.*, 1962]; in the weak magnetic field of the South Atlantic Magnetic Anomaly (SAMA) region, these protons dip so close to the Earth that the POES spacecraft pass through them. As this signature is not relevant to the determination of activity dependent geomagnetic latitude cutoffs we remove all observations in the SAMA region so that only SPE-produced protons are present in the data.

2.2 Geomagnetic Indices and Solar Wind Observations

Geomagnetic indices provide a measure of the variation of the geomagnetic field, and the storm state. It has previously been shown that variations in solar proton geomagnetic cutoffs track with the variations in the Kp and Dst geomagnetic indices [*Leske et al.*, 2001; *Rodger et al.*, 2006], as expected from theoretical modeling [*Smart et al.*, 2003]. For our study geomagnetic indices have been sourced from the Space Physics Interactive Data Resource (SPIDR, spidr.ngdc.noaa.gov/) and the World Data Center WDC for Geomagnetism, Kyoto.

2.3 Solar Proton Events

In this study we consider SPE's from October 2003 through to April 2012. As our goal is to determine polar rigidity cutoffs, we limit ourselves to the larger SPE's in this time window, using the list provided by NOAA (available at http://www.swpc.noaa.gov/ftpdir/indices/SPE.txt) which provides the >10 MeV proton flux observed at geostationary orbit over the time period 1976-present. Note that an SPE in this list is defined as spanning the time from when the flux climbs above 10 pfu (where pfu is the proton flux unit [protons·$s^{-1}sr^{-1}cm^{-2}$ for >10 MeV protons measured at geostationary orbit]) to when the flux again falls below this value. In some cases, several discrete solar proton injections into the interplanetary medium can occur within one of the listed NOAA events; examples of this occurred in October 1989, October 2003, and January 2005. Table 3 lists the

15 SPE we include in this study. Note that the two very large events in early 2012 are included amongst the largest 15 SPE (in terms of >10 MeV flux) which occurred in the last ~37 years, as is January 2005 and October 2003. In addition to the 15 listed in Table 3 there were 17 smaller SPEs during the time range investigated which we did not include as their >10 MeV proton flux at GOES was usually well under 350 pfu. Table 3 gives the start time of the SPE, the GOES >10 MeV Proton Flux, information on associated Coronal Mass Ejections (CME), and the number of POES spacecraft operating during each SPE. The SPE start time and CME observations are the date and time of the events in day/time format. The number of POES spacecraft operating during each SPE is also shown as an indication of amount of rigidity cutoffs likely to be obtained. The words 'East' and 'Halo' are used to describe the CME direction. The 'Earth-directed' CMEs are called 'Halo' as they appear as a bright halo around the Sun in visual detectors.

3. Determination of Rigidity Cutoffs

3.1 Finding cutoffs from POES observations

In order to determine the geomagnetic latitude of the rigidity cutoff, we primarily follow the process followed by *Leske et al.* [2001] who examined SAMPEX data. This takes the average proton flux observed above 70° magnetic latitude (an *L*-shell value of 8.5) and sets the rigidity proton cutoff point as the location where the proton flux is half of the average value, which we term the "cutoff flux". From the cutoff flux location we determine the IGRF *L*-shell of the rigidity cutoff from the satellite orbit information. The rigidity cutoff location is determined separately for passes entering and leaving the polar regions, and independently for each hemisphere and each satellite to produce the highest time resolution possible. In order to discriminate between the satellite entering the magnetic polar region and exiting, we find the maximum magnetic latitude for that pass, and split the orbit into two around that point.

In general the approach put forward by *Leske et al.* works well as the proton fluxes across the pole usually show a consistent pattern; very little (or no) flux at low *L*-shell values followed by a steep (almost vertical) increase around the cutoff location followed by a more or less constant high flux through the polar region. However, on occasions the proton fluxes observed in the satellite data at high latitudes display irregularities, either abruptly falling below the average polar cap proton flux value for a short period or rising greatly above the average, which will lead to significant errors in the automatic determination of the rigidity cutoff location (an example of which is given below).

We therefore applied an additional test to the rigidity cutoff location algorithm. A small increment in flux about the cutoff flux value is selected. If no values are found to be within this range the range is increased until an appropriate cutoff value is found. To make sure that this value is the correct cutoff flux value, a larger increment about the cutoff flux value was taken and a second *L*-shell value found, representing the cutoff location for the second test. The two *L*-shell values were compared. If there was a large difference (>0.2 *L*) between the two *L*-shell values it was assumed that the first cutoff value found was not correct. The increment is slightly increased and the method repeated until a cutoff was correctly found with a small difference in *L*-shell values between it and a larger increment about the proton cutoff value. The *L*-shell difference is taken to be small because the gradient of proton flux is almost vertical near the cutoff and a small change in *L*-shell value produces a large change in proton flux. Upon application of this process, we find that two further tests are required to improve our detection of the cutoffs. These are 1). ensuring that the proton flux increases with increasing *L*-shell (i.e., testing the slope), and 2). checking that the cutoff detected is the most equatorward sudden flux change. We find that these additional tests are useful when there are large irregularities in the flux (for example, as seen in Figure 3b). Manual examination of the SPE passes show that the modified algorithm picks out the correct cutoff values near the middle of the rising/falling flux edge most of the time, and hence was applied to our large dataset of POES passes during which SPE were taking place. Once a rigidity cutoff is determined, we associate a Kp and Dst value with the time of the observed cutoff by interpolating geomagnetic indexes from their native resolution (Kp: 3 hours, Dst: 1 hour) into the rigidity cutoff timings which have 1 s resolution. We remove unphysical values which arise from the interpolation (for example, Kp values less than zero).

Figure 3 shows examples of the rigidity cutoff IGRF L-shells determined for two satellite passes where the proton fluxes across the poles is well behaved (upper panel) such that the *Leske et al.* [2001] approach may be applied directly, along with an example where the fluxes vary rapidly with time/space across the polar cap (lower panel), where the modified algorithm is required to determine the IGRF *L*-shell of the rigidity cutoffs. This is an example where abrupt changes in the proton flux can produce highly unrealistic cutoffs. In the second case a "naïve" application of the simple algorithm could produce a rigidity cutoff for entering the pole at about L=34, vastly different from the true value near L=4.5.

By applying our algorithm to all 15 SPE listed in Table 3, we find a total of 18,526 proton rigidity IGRF *L*-value cutoffs of which 8579 are for the lowest energy range. Note that these values are for Dst, when considering Kp there are 182 fewer points due to the removal of unphysical Kp values. Note that it is possible for the $P7_{omni}$ -$P6_{omni}$ (24.3 MeV) energy range to produce a good cutoff value while higher ranges do not, due to the much lower POES-observed fluxes with increasing energy.

4. Time Variation of Rigidity Cutoffs

Figure 4 shows the time-varying proton cutoff values (circles) determined from the POES $P7_{omni}$ -$P6_{omni}$ (24.3 MeV) observations during the large SPE which occurred in late January 2012. Here the cutoffs from all 6 spacecraft are combined for both hemispheres, leading to a very high time resolution. The gap in cutoff values around 27 January occurs due to the proton flux falling to levels too small to provided detectable cutoffs.We plot the cutoffs against the invariant latitude determined from the IGRF *L*-shell as the data is well organized in this coordinate. Overlaid on this plot is the geomagnetic indices (dashed line), Kp for the top panel and Dst for the lower panel. The right hand side y-axis limits have been adjusted to centre the geomagnetic indices over the time-varying cutoffs to demonstrate the good agreement between the time variation in the cutoffs and the indices. Invariant latitude ϕ can be calculated from the *L*-value through the equation

$$\phi = \cos^{-1}(\sqrt{1/L}) \quad (1)$$

As reported previously, Figure 4 confirms that the variations in solar proton geomagnetic cutoffs track with the variations in the Kp and Dst geomagnetic indices. When Kp increases or Dst decreases (i.e., increasingly levels of "storminess") the cutoff levels move to lower geomagnetic latitudes, i.e., equatorward. However, there is a very strong shift polewards around 15:00 UT on 24 January 2012, at a time when Dst becomes strongly positive. An examination of the individual satellites passes at this time shows that the rigidity cutoffs on the Sun-facing side of the Earth are shifted poleward, with the *L*-shells of the cutoffs on the Sun-facing side being almost twice that than on the anti-Sun side. The timing of this feature, as well as the positive Dst values at this time, are both consistent with the impact of an Interplanetary Coronal Mass Ejection (ICME), compressing the geomagnetic field on the Sun-facing side of the Earth and pushing the rigidity cutoffs poleward on the Sun-side for a short period (~4-5 hours). This effect has been previously noted for the January 2012 SPE [*Tyssoy*, 2012], and we find it is a common, if short-lived, feature during the SPE we consider in this study.

As noted by *Leske et al.* [2001] the variations in Kp appear to lead the variations in the proton cutoffs, while Dst appears to be near simultaneous. These authors also suggest that Kp may represent the variations better than Dst. We consider the possibility of time offsets and the quality of the two parameters in the next section.

5. Empirical Fitting of Rigidity Cutoffs

In this paper our goal is to provide empirical expressions to predict the geomagnetic latitudes most likely to be affected by PCA during SPE, and how these limits will vary with geomagnetic activity. In particular, we hope to provide simple relationships which might be used by the aviation industry when considering polar flight routes. The primary contributors to PCA are protons with energies near 20 MeV [*Patterson et al.*, 2001], and as such the POES $P7_{omni}$-$P6_{omni}$ (24.3 MeV) observations should provide the best estimates from the observations we have available. We therefore undertake empirical fitting of the variation of the proton rigidity cutoffs with geomagnetic activity, focusing on the lower energy passband. For completeness we also undertake the same fitting for the higher energy passbands as given in Table 2.

Our first step was to test the concept of time offsets between the rigidity cutoffs and the geomagnetic indices, as seen in Figure 4. We undertook naive fitting between the cutoffs and the indices using a polynomial expression and determining the coefficient of determination (R^2) to determine the quality of the fitting. By applying time offsets to the geomagnetic indices we found that the best fit (i.e., best R^2 value) occurred when Kp was shifted forward in time by slightly over 3 hours, i.e., that variations in Kp occur ~3 hours before the associated change in the proton cutoffs. As an alternative approach and to provide additional confidence in the R^2 result, we also checked for valid time shifts using a cross-correlation approach. In this case we found that the cross-correlation typically peaked when the Kp was shifted forward in time by slightly under 3 hours. In the case of Dst the best R^2 value occurred when the Dst values were timeshifted backwards by slightly more than 1 hour, i.e., the Dst variations typically occur after the associated change in the cutoffs. However, when testing this timeshift using cross-correlations the R^2 result was not supported, and therefore we do not timeshift the Dst dataset. For simplicity we have rounded the Kp time shifts to the native time step of this geomagnetic index (i.e., 3 hours in

Kp). Thus from this point on the Kp expressions will describe a rigidity cutoff value 3 hours in the future. Note that our results are again consistent with *Leske et al.* [2001], who noted that Kp appeared to lead the changes in proton cutoffs.

5.1 Transforming cutoffs to different altitudes

Proton cutoffs depend on the rigidity of the protons and the geomagnetic field. However, as the magnetic field changes with altitude over a given location so does the rigidity cutoff. In order to apply the cutoffs found at POES altitudes to the atmosphere we need to transform the cutoff values appropriately. Here we follow the approach outlined by *Smart and Shea* [2003] using the IGRF determined L-value. This exploits the basic relationship between the geomagnetic rigidity cutoffs R_c and L, i.e.,

$$R_c = V_k L^{-2} \qquad (2)$$

where V_k is an altitude independent constant. Thus by knowing the value of V_k for the IGRF L-value at 835 km altitude above a given location, one can determine R_c at 100 km once one knows the L-value for that location at 100 km altitude. A proton which can just reach POES satellite altitudes, i.e., at the cutoff, will not penetrate to 100 km altitude. We therefore transform the POES passbands to 100 km, to show the representative energy range for the empirical fits transformed to 100 km.

5.2 Removal of data points

The impact of ICME briefly moves the cutoffs substantially polewards. As seen in Figure 4, this cannot be represented by the Kp-variation at all, and is poorly described by the Dst variation. It also only affects the Sun-side orbits, and hence is strongly magnetic local time specific. As our goal is to provide simple empirical expressions for the rigidity cutoffs, we remove the time periods affected by CME using the NOAA RSGA sudden impulse times (http://www.swpc.noaa.gov/ftpmenu/forecasts/RSGA.html) and defining the ICME affected period as being 15 min before and 6 hour after the impulse. This removes 1299 cutoffs for the lowest passband, i.e. about 8% of the data demonstrating it is a second-order effect. However, we note that for some applications the examination of ICME impacts upon the rigidity cutoffs should be of further interest, for example for improving our understanding of the distortion of the geomagnetic field at these times. In an operational sense it might be possible to include the effect of ICME pushing the sunward-side rigidities polewards by ~5° by producing Dst-dependent fits for different magnetic local times. We have not undertaken this as it appears to be a second-order effect.

Errors in the rigidity cutoff algorithm produce a small number of clearly spurious points at very high latitudes. The inclusion of these highly scattered points in the empirical fitting produced curves which were offset polewards by about 2 degrees relative to the majority of the dataset. We therefore simply removed any rigidity cutoffs with geomagnetic latitudes over 66º (only about 200 cutoffs were removed at this step, across all energy passbands). After this there are 7683 invariant latitude rigidity cutoffs in the lowest energy passband for fitting against Kp and 7791 for fitting against Dst. Again, the difference in the number of Kp and Dst-linked cutoffs comes from the removal of unphysical Kp values.

5.3 Empirical fitting

Initially, we considered whether to assume a linear, quadratic, cubic or quartic relationship to fit the proton cutoffs to the geomagnetic indices (time-shifted for the case of Kp). Least-squares fitting was undertaken between the POES-derived invariant latitude of cutoff and the geomagnetic index using the commercial software product MATLAB. On the basis of the observed relationships in the data and the fit, we concluded that a quadratic provided the most sensible fit to Kp, while a linear relationship worked best for Dst. Note that the quadratic relationship we assume for fitting to Kp-relationship is somewhat consistent with the forms found from the modeling of *Smart and Shea* [2003]. Thus for clarity the relationships to determine the IGRF invariant latitude for the rigidity cutoff is given by:

$$A\,Kp_{shift}^{2} + B\,Kp_{shift} + C = \text{IGRF invariant latitude of cutoff} \qquad \text{(degrees)} \qquad [1]$$

$$B\,Dst + C = \text{IGRF invariant latitude of cutoff} \qquad \text{(degrees)} \qquad [2]$$

where A, B, and C are the empirical fitting parameters, Dst is the geomagnetic index, and Kp_{shift} is the time-shifted geomagnetic index.

When undertaking our fits, we initially treated each hemisphere separately. We found a small but consistent offset between the northern and southern hemisphere data, where the southern hemisphere cutoffs were located about 0.5 degrees equatorwards of the northern values. This may reflect a consistent issue with the IGRF model, although we acknowledge this seems unlikely given the development invested in that model. Nonetheless, this offset is vastly less than the scatter in the cutoff data, and thus we combine the observations from the two hemispheres in order to produce best fits.

Figure 5 presents the distribution of rigidity cutoffs observations with geomagnetic index, which we use to produce our empirical fits. Note that these distributions are for the lowest energy passband (~37 MeV at 100 km altitude). As expected, there are considerably fewer cutoffs for highly disturbed conditions (Kp>7 or Dst <-100 nT).

Table 4 provides the empirical fitting parameters for the 3 passbands we consider, for both Kp (upper section) and Dst (lower section). As can be seen from the correlation coefficient (r) and coefficient of determination (R^2) values, the variations in Kp provide slightly better fits than Dst. This is fortunate in an operational sense, as the time shifts indicate that Kp can be used to predict the future behavior of the rigidity cutoffs. As expected, the correlation coefficient values indicate that the non-time shifted Kp values produce a slightly lower quality correlation coefficient (~0.07 lower) than the time shifted case given in Table 4. While the number of data points available in the fitting decreases with increasing energy (as there is significantly less flux at higher energies), the fitting quality actually improves with increasing energy. The **Δ** parameter in the table is the estimate of the standard deviation of the error. As expected, Table 4 shows that the higher energy protons penetrate to lower geomagnetic latitudes, i.e., closer to the equator. Note that the correlation coefficient (*r*) values given in Table 4 are quite similar to those reported by *Leske et al.* [2001], which were 0.76 for Dst and -0.77 for Kp.

Figure 6 shows the variation of the rigidity cutoff invariant latitudes with Kp determined from the POES observations in the lowest passband we consider. Overplotted (blue line) is the suggested empirical fit using the parameters in Table 4, and the predicted cutoff invariant latitudes (black line) derived from the modeling of *Smart and Shea* [Fig. 1, 2003]. The error bars on the empirical fittings are provided from the Δ from Table 4. While the predicted cutoffs from the *Smart and Shea* [Fig. 1, 2003] modeling lie within the error bars of our empirical fitting from Kp = 0 to Kp = ~8, there is a clear equatorward offset, suggesting a systematic offset between the two. It appears that for most geomagnetic activity levels solar protons generally penetrate ~1-2º further equatorward in our empirical study than is predicted by Smart and Shea. As our proton observations are determined from energy passbands, one might imagine that the ~1-2º latitude offset might arise from the energy widths (e.g., Table 2). However, we can test this by contrasting our curves with the Smart and Shea predictions for the upper and lower energy limits of the passbands, rather than the logarithmic mean energy. We find that this shifts the Smart and Shea cutoffs by approximately ±0.5º around the curve shown in Figure 6, and thus cannot explain a systematic offset. The empirical fit and the Smart and Shea curves in Figure 6 agree best around Kp=7, after which the *Smart and Shea* [Fig. 1, 2003] modeling seems to overpredict the equatorward shifting of the cutoffs at the highest Kp storm-levels. While the number of POES observations at these very high Kp are comparatively small, and the scatter in the POES-derived cutoffs large, our rigidity relationship is consistent with the earlier findings of Rodger et al. [2006] and *Clilverd et al.* [2007]. Using ground-based observations those authors suggested that the *Smart and Shea* modeling over-predicted the equatorward shift for Kp>7, with much smaller shifts more likely for those very disturbed conditions. However, in the strictest sense our observations do confirm the validity of the *Smart and Shea* [2003] modeling for most geomagnetic storm Kp ranges as the line lies within the uncertainties, and the general behavior of the two curves is similar over a wide range of Kp values.

5.4 Testing of Predictive Ability

As an indication of the ability of the empirical expressions to fit the time-varying rigidity cutoffs, we excluded the observations from the two March 2012 SPE and fitted only the POES cutoff observations for the first 13 SPE. The top panel of Figure 7 shows the lower passband rigidity cutoff observations for March 2012 in much the same format as Figure 4. This figure includes the predicted cutoffs using Kp (dashed black line) and Dst (blue solid line), for the fitting using the 13 SPE. Clearly the empirical expressions do a reasonable job of predicting the invariant latitudes of the cutoffs, even though this SPE was not included in the 13 SPE analysis. The lower panel of Figure 7 indicates the predicted cutoffs when all 15 SPE are included in the determination of the empirical parameters; as there were a large number of satellites operational by March 2012 these two SPE contributed a large number of cutoffs (982 or ~12% of the total cutoff observations for the lowest passband), leading to small changes to the time-varying behavior of only a few tenths of a degree at most. In practice the large number of additional cutoffs provided by the March SPE do not make a significant change to the fitted expressions given in Table 4. This demonstrates both that there is a reasonably consistent response in terms of geomagnetic variability and rigidity cutoffs from SPE to SPE, and that our empirical expressions capture a reasonable fraction of this variability. Note, however, that the satellite-determined cutoffs shown in Figure 7 vary over ~2 degrees of IGRF determined invariant latitude, which is similar to that reported by *Leske et al.* [Fig. 5, 2001]. The size of this band may indicate inaccuracies in our approach for determining the cutoffs, but may also be influenced by inaccuracies in this magnetic field model.

6. Variation of PCA Regions with Geomagnetic Activity

Using equation 1 and the empirical fitting parameters in Table 4 we can predict the high latitude regions in which it is likely that HF communications will be badly affected by PCA during solar proton events. The left hand panels of Figure 8 shows a map of the northern hemisphere (top) and southern hemisphere (bottom) with the geomagnetically-dependent PCA limits overplotted. With increasing storm-intensity the limits move equatorwards, with the shift from Kp=1 to Kp=7 spanning ~850 km. As in Figure 2, the magenta dashed line marks 82° latitude, above which geostationary satellite communications are unavailable. Comparing Figure 8 with Figure 2 it becomes clear that very significant fractions of the flight path from the eastern airports of North America to North Asia will likely be affected by PCA, and that it would be very difficult to reroute the paths to entirely avoid the affected zone. Even with the availability of SATCOM the March 2012 SPE HF communication disruptions caused Arctic air traffic centers to alter aircraft separations and for airlines to move paths ~10° southwards of the SATCOM latitude limit [*Federal Aviation Administration*, 2012]. In contrast, in the Southern Hemisphere it seems more possible to mitigate these effects by choosing more equatorward routes (excepting flights to the Antarctic), albeit with increases in fuel burn and hence flight cost.

Figure 6 shows that there is significant scatter in the POES-detected rigidity cutoffs, and the empirical fitting undertaken above produces curves which pass through the middle of the cutoff data. Operationally, one may wish to take a conservative approach and consider the equatorward edge of the POES-detected rigidity cutoff observations to define the equatorward edge of the PCA affected region. We suggest this can be best done by decreasing the value of

C in Table 4 by 2°, selected from the size of the envelope seen in Figure 6. This produces the "shifted" maps shown in right-hand panel of Figure 8.

7. Discussion

In the US National Research Council report on understanding the societal and economic impacts of severe space weather, information on the need for timely information on PCA events were provided by Michael Stills of United Airlines. To quote from this report: “It is very important to have it in a timely fashion and as far in advance as possible. Clearly we realize there are limitations, but to have from an infrastructure standpoint a forecast, say, 6 to 10 hours in advance would be wonderful, but from an operational and planning standpoint, we are probably looking at a minimum of, say, 3 to 4 hours in advance, where we can make a tactical decision and still feel confident in the operation.” [*National Research Council*, Pg. 51-52, 2008]. Once an SPE is confirmed, we have found that the Kp parameter provides ~3 hours of predictive possibility. While the "true Kp" is not available in real time in practise, there are real-time estimated Kp values. One example is the Wing Kp Predicted Geomagnetic Activity Index model [*Wing et al.*, 2005], which is now operational at NOAA and available through this website: http://www.swpc.noaa.gov/wingkp/. We compared the true Kp with the Wing model predictions for the time period 16 February 2011- 30 June 2012 and found there is a quite good correlation between the two. The Wing Kp provides a 1-hour forward prediction and a 4-hour forward prediction, each with 15 min time resolution. In this time period the predictions showed correlation coefficients with true Kp of 0.67 and 0.60, respectively. We also tested the output of the Wing model for the January and March 2012 SPEs, comparing the cutoffs from the true Kp with the 1-hour and 4-hour predicted Wing Kp. For these events there are significant time periods in which the quality flag ID provided by the Wing

Kp model indicates that the outputs are bad due to problems with the ACE spacecraft observations used in the model. This affects 35.5% of our proton cutoffs for these SPE, although it only affects 2.4% of the 500 day time period (Feb 2011-June 2012). In the time periods for which the Wing model output is "good/nominal" the correlation coefficient for these SPE events is 0.5072 for the Wing model 1-hour predictions and the lower energy passband cutoffs, including the 3-hour time shift found in section 5, thus providing a prediction of the cutoffs 4 hours in advance. In contrast the correlation coefficient for the Wing Kp model 4-hour predictions is 0.5685 (providing a proton cutoff prediction 7 hours in advance), suggesting that both outputs of the Wing model could be usefully used. We caution that while the correlation coefficient for the 4-hour model outputs is better than the 1-hour model, these correlations are based on only ~1100 data points. The fact that the 4-hour model has a lower correlation to "true Kp" across the much longer 500 day period indicates care should be used, and a larger study involving cutoffs and Wing Kp model output is warranted. As the output of the Wing Kp model is available in real time online, the combination of the 1-hour or 4-hour Kp prediction and the 3-hour time offset suggests that a minimum of ~4 hours of prediction is possible in operations, allowing "tactical" decisions. NOAA is also providing Kp-predictions further into the future with 2-3 day forecasts now online (http://www.swpc.noaa.gov/ftpdir/latest/three_day_forecast.txt). This should provide the level of predictive warning suggested above, assuming that quality predictions of solar proton events can also be generated. Obviously, this is still an active research area.

In our study we have focused on the link between the Kp geomagnetic index and the change in solar proton access to the polar atmosphere. To a lesser extent we have also considered the Dst index. Estimates of both of these indices are available in near real-time, and some predictive models have been developed. There are, however, a wealth of additional geomagnetic indices available which may also produce good representations of the changing proton rigidly cutoffs. While we have chosen to work inside the approach favored in the literature to date such that we can make comparisons with the work of others (and most especially Smart and Shea) we note that considering a wider range of indices might lead to improved results. This is worthy of future research.

At this time NOAA provides estimates of SPE produced HF blackouts in the polar regions with the Space Weather Prediction Center (SWPC) D Region Absorption Predictions (D-RAP) model (online at http://www.swpc.noaa.gov/drap/index.html) as an operational product. The SWPC D-RAP calculates HF absorption in the polar regions using observed GOES energetic proton fluxes, combined with the Smart and Shea Kp-dependent model to determine the latitudinal boundaries for the region affected. Our study provides a test of the Smart and Shea boundaries produced from geomagnetic modeling. On the basis of the POES-observed cutoffs presented here, we suggest that the Smart and Shea boundaries should be shifted equatorwards by ~1.5°, which will provide a better estimate of the boundary location for geomagnetic disturbances less than Kp<7. For higher Kp-values Smart and Shea predict more extreme equatorward shifts than observed, although the scatter is rather high at these times. Given the size of error bars seen in Figure 6, one can conclude that the Smart and Shea Kp-dependent boundaries used in the current operation model are valid for most storm conditions. A simple improvement to the operational model would be to use the time shifted predicted Kp and the ~1.5° latitude shift with the existing boundary.

Operationally the commonly used definition for a solar proton event is the time period over which the GOES-detected >10 MeV proton flux is larger than 10 proton flux units (pfu). In practice other instruments are more or less sensitive than this definition. For example, D-region observations made using subionospheric VLF propagation experiments indicate that detectable propagation changes occur when solar protons strike the ionosphere where the incoming flux at GOES is <10 pfu [*Clilverd et al.*, 2006a, b]. However, the instruments on POES observe considerably lower flux than GOES. The proton flux counts observed at POES altitudes are considerably lower than at GOES (~35,800 km altitude), in large part due to the shielding of the geomagnetic field. A SPE observed as having ~10 pfu in GOES data is indistinguishable from noise at POES altitudes in the proton observations. For fluxes of a few 100 pfu at GOES the proton cutoffs can be visually observed in POES data but remain close to the noise levels, making them difficult to automatically detect. This is the primary reason for the selection of SPE to produce the events in Table 3. The electron telescopes in the MEPED detector suffer from proton contamination [*Yando et al.*, 2011], such that electron observations in the polar cap during SPE and at all times in the SAMA are totally unreliable. It appears reasonable to assume the electron telescope data are certainly contaminated when the omni-directional proton detectors observe an SPE, which will make it extremely difficult to study electron precipitation during solar proton events [e.g. *Funke et al.*, 2011].

8. Summary and Conclusions

In this paper we have exploited the observations from a large number of satellites in low-Earth orbit to produce a large set of proton rigidity cutoffs sorted by IGRF *L*-shell (and hence invariant latitude). We examine 15 large SPE that occurred from October 2003 through to April 2012, during which at least 3 up to as many as 6 POES spacecraft were operational. As expected from earlier studies, and theoretical modeling, we find the rigidity cutoff latitudes are well organized by the geomagnetic indices Kp or Dst, evidenced by high correlation coefficients. We find that the Kp index provides a good prediction of the proton cutoff in ~3 hours time (i.e., one time step for the time resolution of Kp).

After excluding cutoffs around the times of ICME impact, we determine empirical fits by which a Kp or Dst value can be used to predict the invariant latitude of the proton rigidity cutoff. We find that Kp produces slightly more reliable correlations than Dst. The expressions from the lowest energy passband provided by the POES MEPED omnidirectional detectors should provide a reasonable estimate for the latitude range over which significant PCA is occurring, and thus the zone in which HF communications will be degraded. With existing real-time Kp estimates a prediction of the cutoff latitudes can be made ~4-7 hours into the future, meeting the minimum planning time indicated by the aviation industry. The empirical expressions should also be useful to those researchers who want to investigate SPE effects in atmospheric chemistry and dynamics, allowing a more realistic description of the particle impact on the polar atmosphere. The Smart and Shea Kp-dependent boundaries currently used in the operational NOAA HF blackout model have been validated through our experimental observations, although we have suggested some small changes which might improve the accuracy of the model.

The expressions describing the changing cutoffs for the lower and middle energy passband should also be useful for research examining the impact of solar protons impacting the mesosphere, and in particular the destruction of the tertiary ozone maxima which has been observed during SPE [*Seppälä et al.*, 2006]. The upper POES energy passband relates to protons penetrating to approximately 30 km altitude. The direct chemical impacts of very large SPE in the stratosphere have been found to be rather small [e.g., Seppälä et al., 2008], except in very extreme cases such as the Carrington event [e.g., *Rodger et al.*, 2008]. Thirty kilometers is too high for most aviation radiation exposure considerations, such that ground level neutron monitors would need to be examined to reflect the access of solar protons to the altitudes of inflight aircraft [e.g., *Matthiä et al.*, 2009]. However, this passband will describe the atmospheric electrical conductivity changes which have been experimentally observed at stratospheric altitudes during SPE [*Kokorowski et al.*, 2012].

The high-time resolution offered by multiple low-Earth orbiting spacecraft has demonstrated the strong distortion of the geomagnetic field on the Sun-facing side due to the impact of ICME. During these time periods we find that the geomagnetic latitude of the rigidity cutoffs on the Sun-side consistently shift poleward (relative to the night-side, and also relative to the pre-ICME observations). This shift lasts ~4-5 hours. As our goal was the production of simple empirical expressions which might be useful to the aviation industry, these periods were removed. However, we note that this effect may be of further interest, for example providing a new way to test our understanding of the distortion of the geomagnetic field at these times.

Acknowledgments. JJN and CJR were partly supported by the New Zealand Marsden Fund. The authors would like to thank the researchers and engineers of NOAA's Space Environment Centre for the provision of the data and the operation of the SEM-2 instrument carried onboard these spacecraft, and the staff of FlightAware of Houston, Texas for providing flightpaths through their website, FlightAware.com.

References

Albersheim, S., and M. Gunzelman (2012), International Effort on Space Wx Impacts Supporting Aviation, presented to 2012 AMS Washington Forum Session 10 on 12 April 2012. Presentation available online from http://www.ametsoc.org/boardpges/cwce/docs/profiles/GunzelmanMark/2012-04-AWF.pdf

Bailey, D. K. (1957), Disturbances in the lower ionosphere observed at VHF following the solar flare of 23 February 1956 with particular reference to the auroral zone absorption, *J Geophys. Res.*, 62, 431-463.

Cameron, D., Delta Reroutes Flights as Solar Storm Hits Earth, *Wall Street Journal*, 25 January 2012. Available online at: http://online.wsj.com/article/BT-CO-20120124-712588.html

Clilverd, M. A., C. J. Rodger, Th. Ulich, A. Seppälä, E. Turunen, A. Botman, and N. R. Thomson (2005), Modelling a large solar proton event in the southern polar cap, *J. Geophys. Res.*, 110(A9), doi: 10.1029/2004JA010922.

Clilverd, M. A., A. Seppälä, C. J. Rodger, P. T. Verronen, and N. R. Thomson (2006), Ionospheric evidence of thermosphere-to-stratosphere descent of polar NOx, *Geophys. Res. Lett.*, 33, L19811, doi:10.1029/2006GL026727.

Clilverd, M. A., A. Seppälä, C. J. Rodger, N. R. Thomson, P. T. Verronen, E. Turunen, T. Ulich, J. Lichtenberger, and P. Steinbach (2006), Modeling polar ionospheric effects during the October-November 2003 solar proton events, *Radio Sci.*, 41, RS2001, doi:10.1029/2005RS003290.

Clilverd, M. A., C. J. Rodger, T. Moffat-Griffin, and P. T. Verronen (2007), Improved dynamic geomagnetic rigidity cutoff modeling: testing predictive accuracy, *J. Geophys. Res.*, 112, A08302, doi:10.1029/2007JA012410.

Cooke, D. J., J. E. Humble, M. A. Shea, D. F. Smart, N. Lund, I. L. Rasmussen, B. Byrank, P. Goret, and N. Petrou (1991), On Cosmic-Ray Cut-Off Terminology, *Il Nuovo Cimento C*, 14, 213-234.

Davies, K. (1990), Ionospheric Radio, IEE Electromagn. Ser., vol. 31, 580 pp., Peter Peregrinus, London.

Dayeh, M. A., M. I. Desai, K. Kozarev, N. A. Schwadron, L. W. Townsend, M. PourArsalan, C. Zeitlin, and R. B. Hatcher (2010), Modeling proton intensity gradients and radiation dose equivalents in the inner heliosphere using EMMREM: May 2003 solar events, *Space Weather*, 8, S00E07, doi:10.1029/2009SW000566.

Evans, D. S., and M. S. Greer (2004), Polar Orbiting environmental satellite space environment monitor - 2 instrument descriptions and archive data documentation, NOAA technical Memorandum version 1.4, Space Environment Laboratory, Colorado.

Fahey, T., and G. Scott, Delta Hazard Avoidance Procedures and Use of Space Weather Information, 2012 Space Weather Workshop Abstracts, pg. 12, 24 April 2012. Available online from http://www.swpc.noaa.gov/sww/SWW_Booklet_2012.pdf

Funke, B., Baumgaertner, A., Calisto, M., Egorova, T., Jackman, C. H., Kieser, J., Krivolutsky, A., López-Puertas, M., Marsh, D. R., Reddmann, T., Rozanov, E., Salmi, S.-M., Sinnhuber, M., Stiller, G. P., Verronen, P. T., Versick, S., von Clarmann, T., Vyushkova, T. Y., Wieters, N., and Wissing, J. M., (2011), Composition changes after the "Halloween" solar proton event: the High Energy Particle Precipitation in the Atmosphere (HEPPA) model versus MIPAS data intercomparison study, *Atmos. Chem. Phys.*, 11, 9089-9139, doi:10.5194/acp-11-9089-2011.

Federal Aviation Administration, Effects of Major Eruption of the Sun in the Cross-Polar Region, The Thirty-Sixth Meeting Of The Informal Pacific ATC Co-Ordinating Group (IPACG/36), May 2012. Available online from http://www.faa.gov/about/office_org/headquarters_offices/ato/service_units/enroute/oceanic/documents/IPACG/IPACG36/IP13_Sun_Eruption.doc

Jackman, C. H., D. R. Marsh, F. M. Vitt, R. R. Garcia, C. E. Randall, E. L. Fleming, and S. M. Frith (2009), Long-term middle atmospheric influence of very large solar proton events, *J. Geophys. Res.*, 114, D11304, doi:10.1029/2008JD011415.

Kavanagh, A. J., S. R. Marple, F. Honary, I. W. McCrea, and A. Senior (2004), On solar protons and polar cap absorption: constraints on an empirical relationship, *Ann. Geophys.*, 22(4), 1133-1147.

Kokorowski, M., A. Seppälä, J. G. Sample, R. H. Holzworth, M. P. McCarthy, E. A. Bering, and E. Turunen (2012), Atmosphere-ionosphere conductivity enhancements during a hard solar energetic particle event, *J. Geophys. Res.*, 117, A05319, doi:10.1029/2011JA017363.

Kress, B. T., C. J. Mertens, and M. Wiltberger (2010), Solar energetic particle cutoff variations during the 29–31 October 2003 geomagnetic storm, *Space Weather*, 8, S05001, doi:10.1029/2009SW000488.

Leske, R. A., R. A. Mewaldt, E. C. Stone, and T. T. von Rosenvinge (2001), Observations of geomagnetic cutoff variations during solar energetic particle events and implications for the radiation environment at the Space Station, *J. Geophys. Res.*, 106(A12), 30,011–30,022, doi:10.1029/2000JA000212.

López-Puertas, M., B. Funke, S. Gil-López, T. von Clarmann, G. P. Stiller, M. Höpfner, S. Kellmann, H. Fischer, and C. H. Jackman (2005), Observation of NOx enhancement and ozone depletion in the Northern and Southern Hemispheres after the October–November 2003 solar proton events, *J. Geophys. Res.*, 110, A09S43, doi:10.1029/2005JA011050.

Matthiä, D., B. Heber, G. Reitz, M. Meier, L. Sihver, T. Berger, and K. Herbst (2009), Temporal and spatial evolution of the solar energetic particle event on 20 January 2005 and resulting radiation doses in aviation, *J. Geophys. Res.*, 114, A08104, doi:10.1029/2009JA014125.

Mertens, C. J., B. T. Kress, M. Wiltberger, S. R. Blattnig, T. S. Slaba, S. C. Solomon, and M. Engel (2010), Geomagnetic influence on aircraft radiation exposure during a solar energetic particle event in October 2003, *Space Weather*, 8, S03006, doi:10.1029/2009SW000487.

National Research Council (2008), Severe Space Weather Events-Understanding Societal and Economic Impacts: A Workshop Report, 144 pp., Natl. Acad. Press, Washington, D. C.

Patterson, D., T. P. Armstrong, C. M. Laird, D. L. Detrick, and A. T. Weatherwax (2001), Correlation of solar energetic protons and polar cap absorption, *J. Geophys. Res.*, 106(A1), 149-163.

Reeves, G. D., T. E. Cayton, S. P. Gary, and R. D. Belan (1992), The great solar energetic particle events of 1989 observed from geosynchronous orbit, *J. Geophys. Res.*, 97, 6219-6226.

Robel, J. (Ed.), NOAA KLM User's Guide, National Environmental Satellite, Data, and Information Service, 2009.

Rodger, C. J., M. A. Clilverd, P. T. Verronen, Th. Ulich, M. J. Jarvis, and E. Turunen (2006), Dynamic geomagnetic rigidity cutoff variations during a solar proton event, *J. Geophys. Res.*, 111, A04222, doi:10.1029/2005JA011395.

Rodger, C. J., P. T. Verronen, M. A. Clilverd, A. Seppälä, and E. Turunen (2008), Atmospheric impact of the Carrington event solar protons, *J. Geophys. Res.*, 113, D23302, doi:10.1029/2008JD010702.

Sauer, H. H., and D. C. Wilkinson (2008), Global mapping of ionospheric HF/VHF radio wave absorption due to solar energetic protons, Space Weather, 6(12).

Seppälä, A., P. T. Verronen, V. F. Sofieva, J. Tamminen, E. Kyrölä, C. J. Rodger, and M. A. Clilverd (2006), Destruction of the tertiary ozone maximum during a solar proton event, *Geophys. Res. Lett.*, 33, L07804, doi:10.1029/2005GL025571.

Seppälä, A., M. A. Clilverd, C. J. Rodger, P. T. Verronen, and E. Turunen (2008), The effects of hard-spectra solar proton events on the middle atmosphere, *J. Geophys. Res.*, 113, A11311, doi:10.1029/2008JA013517.

Smart, D. F., and M. A. Shea (1985), A simplified model for timing the arrival of solar flare-initiated shocks, *J. Geophys. Res.*, 90, 183-190.

Shea, M. A., and D. F. Smart (1990), A summary of major solar proton events, *Solar Phys.*, 127(2), 297-320.

Smart, D. F., and M. A. Shea (2003), The space developed dynamic vertical cutoff and its applicability to aircraft radiation dose, *Adv. Space Res.*, 32(1), 103-108.

Smart, D. F., M. A. Shea, M. J. Golightly, M. Weyland, and A. S. Johnson (2003), Evaluation of the dynamic cutoff rigidity model using dosimetry data from the STS-28 flight, *Adv. Space Res.*, 31(4), 841–846.

Störmer, C., (1930) Periodische Elektronenbahnen im Feld eines Elementarmagnetron und ihre Anwendung auf Bruches Modellversuche und auf Eschenhagens Elementarwellen des Erdmagnetismus, *Zeitschr. f. Astrophys.*, 1, 237-274.

Tsyganenko, N. A., Determination of magnetospheric current system parameters and development of experimental geomagnetic models based on data from IMP and HEOS satellites, *Planet. Space Sci.*, 37, 5-20, 1989.

Tyssoy, H. N. (2012), Proton Precipitation into the Mesosphere as deduced from GOES and NOAA/POES Measurements during a SEP Event in January 2012, 4th International HEPPA Workshop in conjunction with SPARC/SOLARIS Abstract Book, Pg. 69.

Vampola, A.L., M .Lauriente, D.C. Wilkinson, J. Allen, and F. Albin (1994), Single Event Upsets correlated with environment, *IEEE Trans. Nucl. Sci.*, 41(6), 2383 - 2388.

Vernov, S. I., I. A. Savenko, P. I. Shavrin, and N. F. Pisarenko (1962), Detection of an inner radiation belt at the altitude of 320 km in the region of the South Atlantic magnetic anomaly, *Planetary and Space Science*, 9(11), 861-865.

Verronen, P. T., A. Seppälä, E. Kyrölä, J. Tamminen, H. M. Pickett, and E. Turunen (2006), Production of odd hydrogen in the mesosphere during the January 2005 solar proton event, *Geophys. Res. Lett.*, 33, L24811, doi:10.1029/2006GL028115.

Wing, S., J. R. Johnson, J. Jen, C.-I. Meng, D. G. Sibeck, K. Bechtold, J. Freeman, K. Costello, M. Balikhin, and K. Takahashi (2005), Kp forecast models, *J. Geophys. Res.*, 110, A04203, doi:10.1029/2004JA010500.

Yando, K., R. M. Millan, J. C. Green, and D. S. Evans (2011), A Monte Carlo simulation of the NOAA POES Medium Energy Proton and Electron Detector instrument, *J. Geophys. Res.*, 116 (A10), doi:10.1029/2011JA016671.

____

J. C. Green, NOAA Space Environment Center, 325 Broadway Blvd., Boulder, Colorado 80305, United States. (e-mail: Janet.Green@noaa.gov)

J. J. Neal and C. J. Rodger, Department of Physics, University of Otago, P.O. Box 56, Dunedin, New Zealand. (email: crodger@physics.otago.ac.nz).

Tables

Satellite	Local Time Ascending Node	Altitude (km)	Data availability
NOAA 15	16:42:14	807	01 June 1998
NOAA 16	20:28:56	849	10 January 2001
NOAA 17	19:12:50	810	12 July 2002
NOAA 18	14:51:13	854	07 June 2005
MetOp 02	21:30:22	817	03 December 2006
NOAA 19	13:33:02	870	23 February 2009

Table 1. An overview of the six satellites carrying the SEM-2 instrument package, including their daytime orbital sector, and date at which they became operational. Note MetOp-2 is a European spacecraft, but carries the same SEM-2 package as the NOAA spacecraft. The local time ascending node is the local time for which the spacecraft are crossing the equator travelling northwards.

Data Channel	Energy Passband (MeV)	Log. Mean at Satellite (MeV)	Log. Mean at 100 km (MeV)
$P7_{omni}$ -$P6_{omni}$	16-35	24.3 MeV	37.2
$P8_{omni}$ - $P7_{omni}$	35-70	51.5 MeV	76.7
$P9_{omni}$ - $P8_{omni}$	70-140	101.0 MeV	151.0

Table 2. The three energy passband determined from the four POES omnidirectional proton channels. The logarithmic mean was taken to determine the approximate centre energy value of the pass band, and this value was transformed to 100 km as described in section 5.1.

SPE Start Time (UT)	>10 MeV Proton Flux units (pfu)	CME observed at the Sun	POES Spacecraft Operational
2012 Mar 13/1810	469	Halo 13/1736	6
2012 Mar 07/0510	6,530	Halo 07/0036	6
2012 Jan 27/1905	796	Halo 27/1827	6
2012 Jan 23/0530	6,310	Halo 23/0400	6
2006 Dec 13/0310	698	Halo 13/0254	5
2006 Dec 06/1555	1,980	Halo	5
2005 Sep 08/0215	1,880	East 07/1723	4
2005 May 14/0525	3,140	Halo 13/1722	3
2005 Jan 16/0210	5,040	Halo 15/2306	3
2004 Nov 07/1910	495	Halo 07/1606	3
2004 Jul 25/1855	2,086	Halo 25/1514	3
2003 Nov 04/2225	350	Halo 04/1954	3
2003 Nov 02/1105	1,570	Halo 02/0954	3
2003 Oct 28/1215	29,500	Halo 28/1054	3
2003 Oct 26/1825	466	Halo 26/1754	3

Table 3. List of SPEs analysis in this study with starting time, the GOES >10 MeV Proton Flux and any associated CME observed at the Sun. The SPE start time and CME observations are the UT date and time of the events in day/time format. The SPE start time is determined as when the >10 MeV flux goes above the 10 pfu level. See text for additional details.

Energy at 100 km (MeV)	**Indice**	***A***	***B***	***C***	***r***	***R*²**	**Δ**	**Data points**
37.2	Kp	-0.057912	-0.38237	63.1626	-0.70679	0.50154	1.72	7683
76.7	Kp	-0.08087	-0.14163	61.712	-0.74373	0.6216	1.3243	4620
151	Kp	-0.083756	-0.06691	59.8825	-0.80126	0.71039	1.1081	4547
37.2	Dst		0.031679	62.5344	0.62563	0.46114	1.7938	7791
76.7	Dst		0.029931	61.3043	0.68625	0.54862	1.4467	4653
151	Dst		0.028514	59.5979	0.73982	0.64016	1.2349	4581

Table 4. Empirical fitting parameters used in equation 1 (for time-shifted Kp) or 2 (Dst) to represent the variation of the rigidity cutoffs geomagnetic invariant latitude at 100 km altitude.

Figures

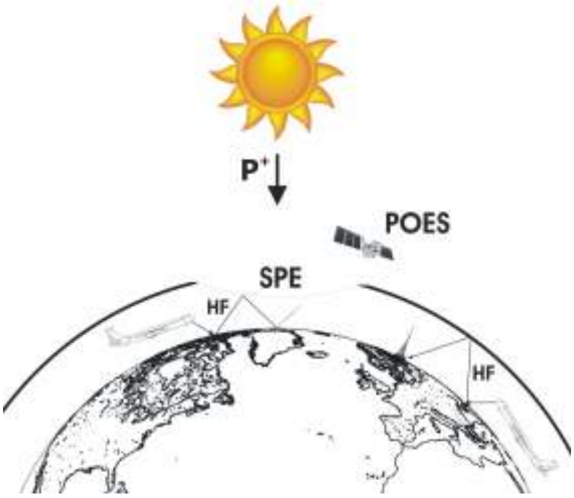

Figure 1. Schematic of the situation considered in this study. Solar protons during a SPE strike the ionosphere, leading to a decrease in the reflection height and an increase in the HF absorption, termed Polar Cap Absorption (PCA). PCA disrupts HF communications in the polar regions, but not at mid-latitude, such that aircraft in the polar regions cannot communicate with HF radio. The edges of the PCA region can be determined by examining the POES spacecraft observations, as their low-Earth orbits carry them through the geomagnetic polar regions.

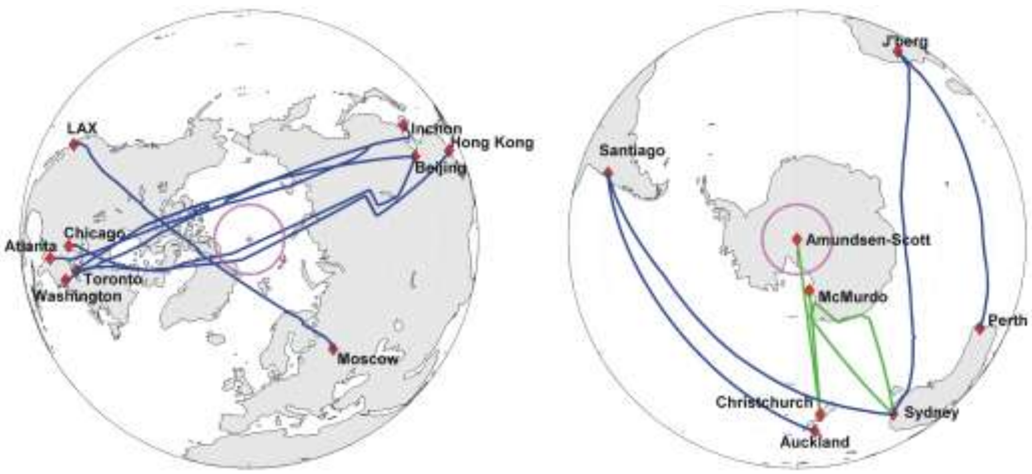

Figure 2. A selection of high-latitude flight paths operated by commercial airlines in 2012. The blue tracks are a selection of actual flight paths taken in mid-late October 2012, while the magenta dashed line marks 82° latitude, above which geostationary satellite communications are unavailable. The green routes in the southern hemisphere paths are great circle routes, but include an indicative route for commercial Antarctic sight-seeing flights operated from Australia. Flights to support the US and New Zealand Antarctic programs are also shown, departing Christchurch, New Zealand. Actual flight paths downloaded from FlightAware.com.

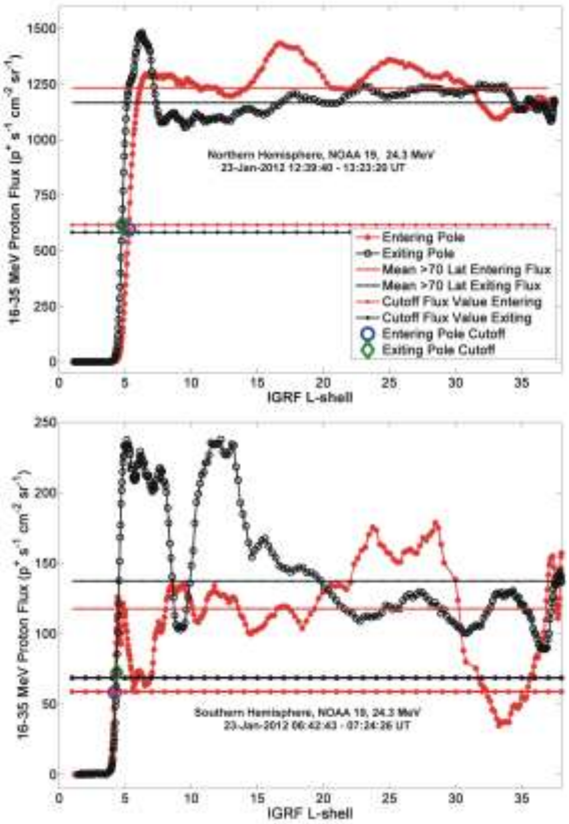

Figure 3. Determining the IGRF rigidity cutoffs from the POES satellite data. The upper panel shows an example where the observed proton flux is "well behaved', and the approach put forward by *Leske et al.* [2001] is appropriate. The lower panel shows a case where the solar proton flux across the pole is more irregular, and the modified algorithm is necessary to produce a reasonable estimate of the cutoff location. In both cases the calculated cutoff point is indicated by the circle and diamond.

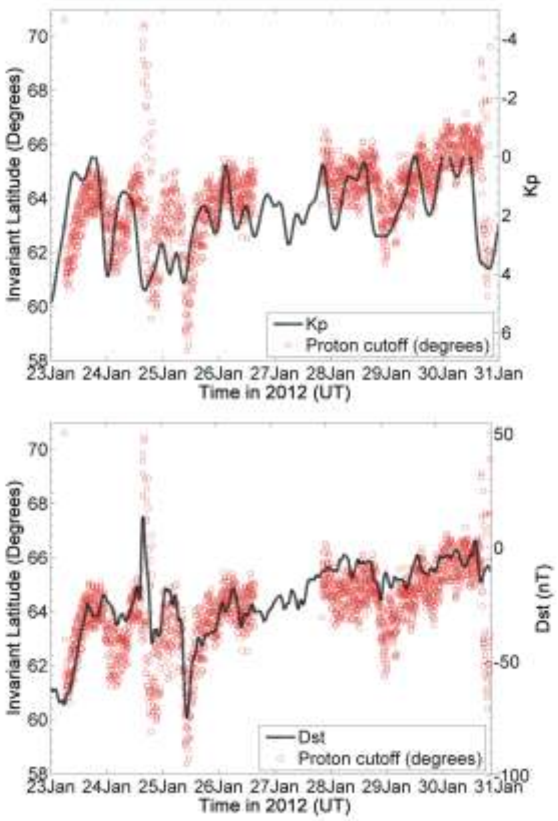

Figure 4. Solar Proton cutoffs for 24.3 MeV protons determined from POES data overlaid with geomagnetic indices for the period 23-31 January 2012. The right hand *y*-axis limits have been adjusted to centre the geomagnetic indices over the time-varying cutoffs. The gap in cutoff values around 27 January occurs due to the proton flux falling to levels too small to provided detectable cutoffs.

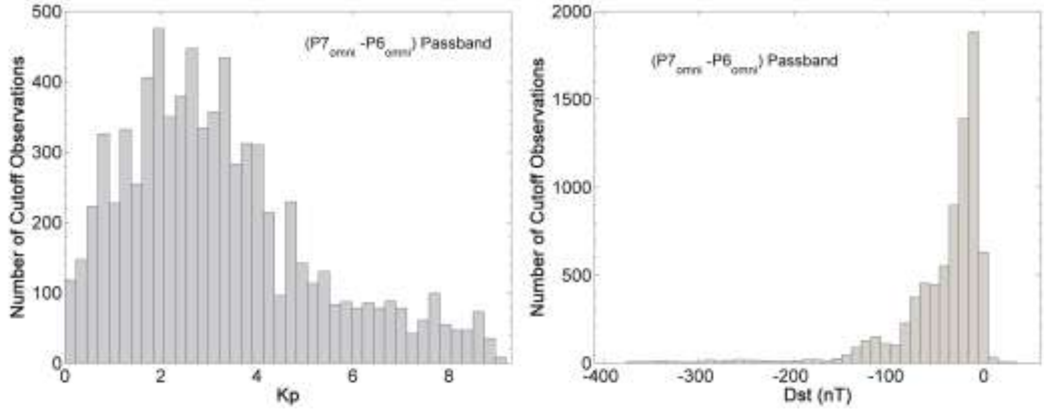

Figure 5. Distribution of rigidity cutoffs observations with geomagnetic index, which we use to produce empirical fits. Note that these distributions are for the lowest energy passband (~37 MeV at 100 km altitude).

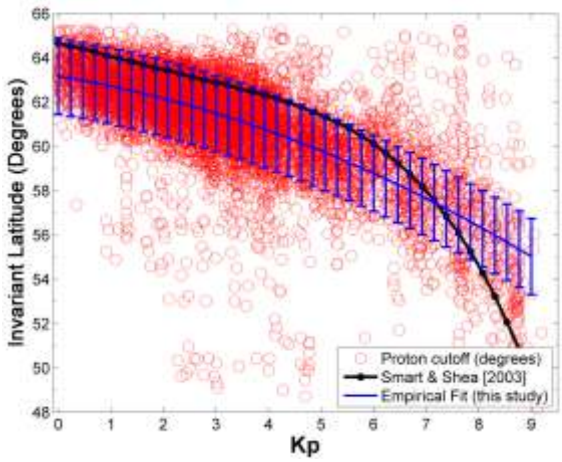

Figure 6. Variation of the rigidity cutoff invariant latitudes with Kp determined for the POES observations (red circles) in the lowest passband we consider. Overplotted (blue line) is the suggested empirical fit using the parameters in Table 4, and the predicted cutoff invariant latitudes (black line) derived from the modeling of *Smart and Shea* [Fig. 1, 2003].

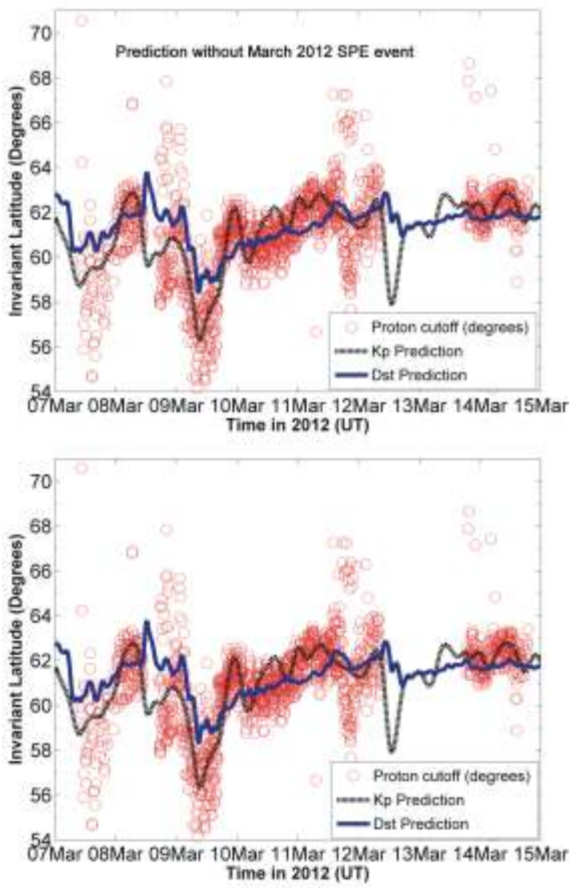

Figure 7. Solar Proton cutoffs for the lowest energy range at 100 km altitude determined from POES data for the period 7-15 March 2012, during which two SPE occurred. The upper panel includes predictions of the rigidity cutoffs by Kp (black line) and Dst (blue line), where the prediction has not involved these SPE (i.e., including only the first 13 SPE in Table 3). The lower panel includes all 15 SPE in the fitting process.

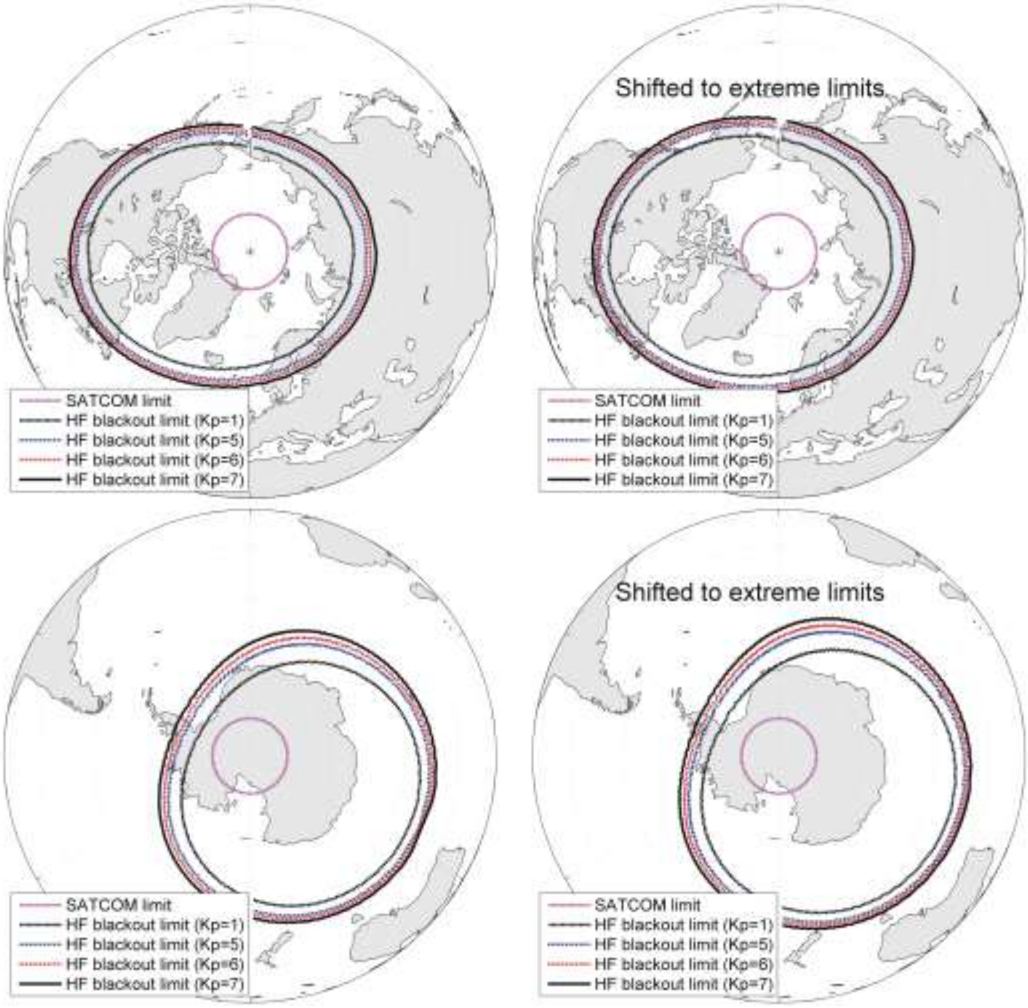

Figure 8. Empirical predictions of the Polar Cap Absorption areas likely to impact HF communications during solar proton events, dependent upon geomagnetic activity. The left-hand panels use the empirical fits from Table 4, while the right-hand panels have a 2° equatorward latitude shift applied to represent the equatorward edge of the POES-detected rigidity cutoffs.

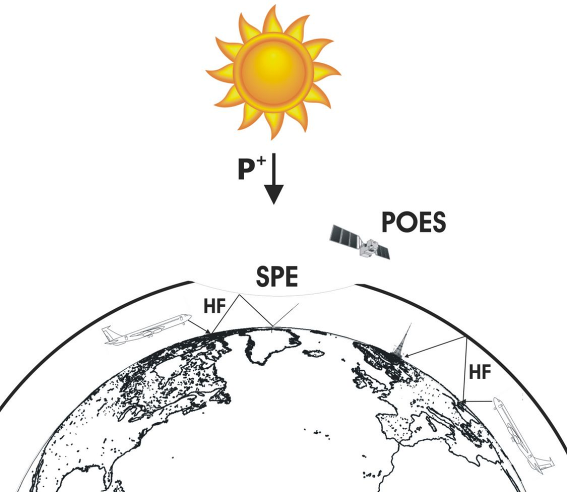

P+
POES
SPE
HF
HF

LAX
Inchon
Hong Kong
Beijing
Chicago
Atlanta
Toronto
Washington
Moscow

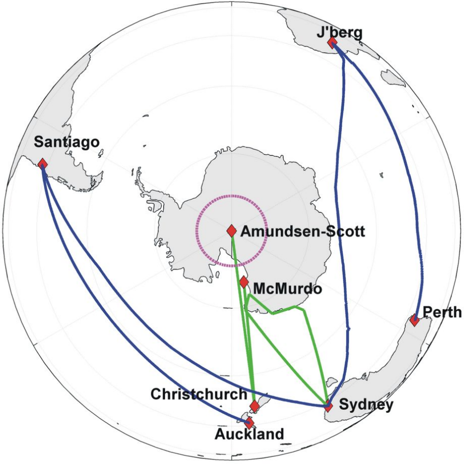

J'berg
Santiago
Amundsen-Scott
McMurdo
Perth
Christchurch
Sydney
Auckland

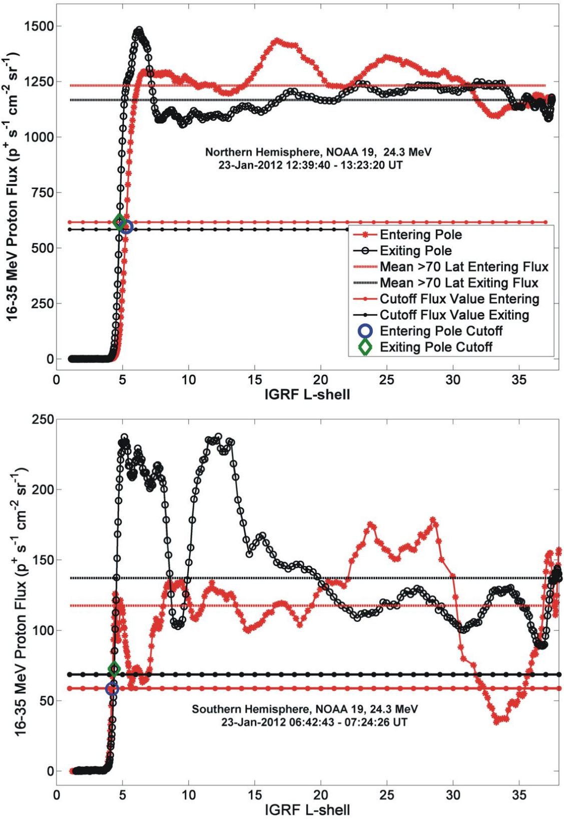
16-35 MeV Proton Flux ($p^+ s^{-1} cm^{-2} sr^{-1}$)
IGRF L-shell
Northern Hemisphere, NOAA 19, 24.3 MeV
23-Jan-2012 12:39:40 - 13:23:20 UT
Entering Pole
Exiting Pole
Mean >70 Lat Entering Flux
Mean >70 Lat Exiting Flux
Cutoff Flux Value Entering
Cutoff Flux Value Exiting
Entering Pole Cutoff
Exiting Pole Cutoff
Southern Hemisphere, NOAA 19, 24.3 MeV
23-Jan-2012 06:42:43 - 07:24:26 UT

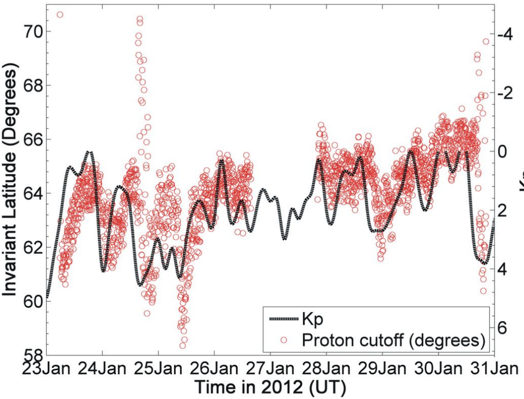

Invariant Latitude (Degrees)
Kp
Kp
Proton cutoff (degrees)
Time in 2012 (UT)
23Jan
24Jan
25Jan
26Jan
27Jan
28Jan
29Jan
30Jan
31Jan

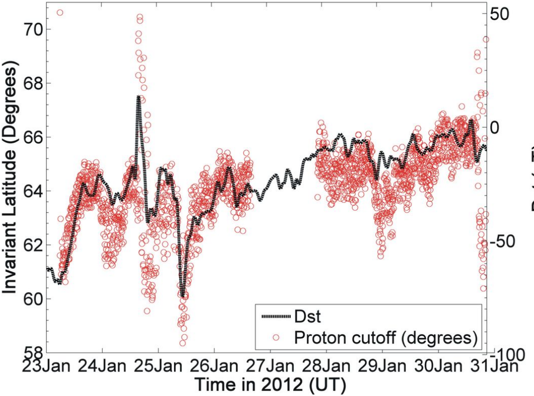

Invariant Latitude (Degrees)
Dst (nT)
Dst
Proton cutoff (degrees)
Time in 2012 (UT)
23Jan
24Jan
25Jan
26Jan
27Jan
28Jan
29Jan
30Jan
31Jan

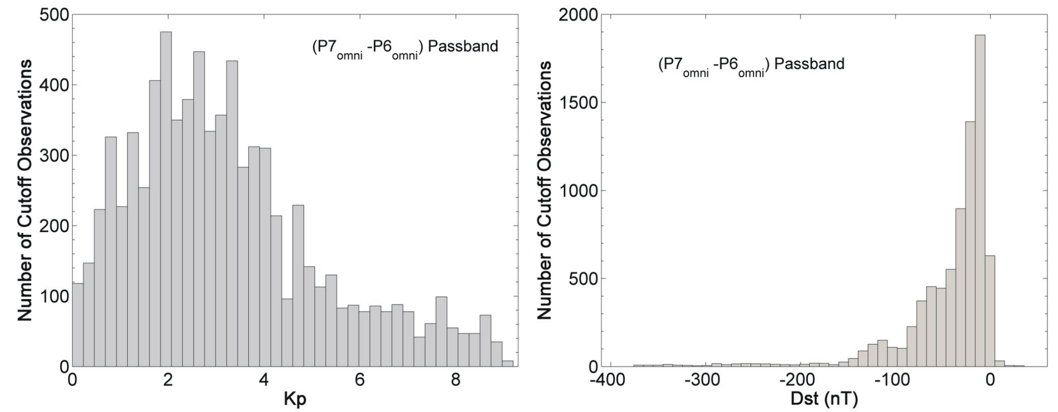

(P7omni -P6omni) Passband
Number of Cutoff Observations
Kp
0
2
4
6
8
100
200
300
400
500
(P7omni -P6omni) Passband
Number of Cutoff Observations
Dst (nT)
-400
-300
-200
-100
0
500
1000
1500
2000

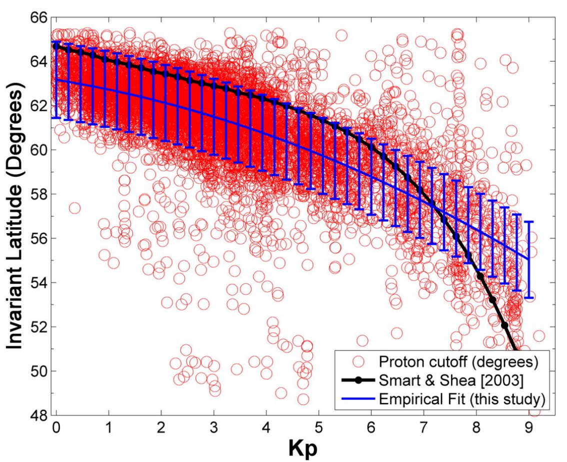

Invariant Latitude (Degrees)
66
64
62
60
58
56
54
52
50
48
0
1
2
3
4
5
6
7
8
9
Kp
Proton cutoff (degrees)
Smart & Shea [2003]
Empirical Fit (this study)

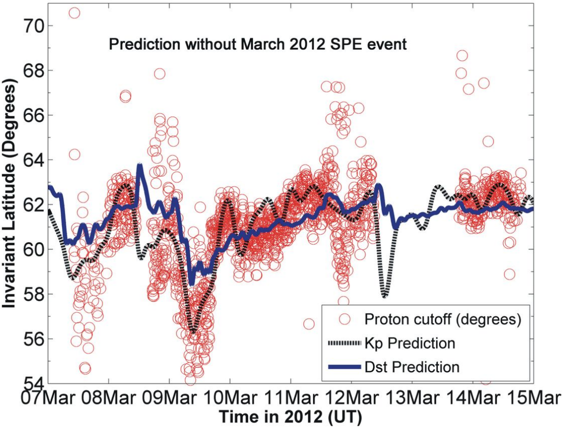
Prediction without March 2012 SPE event
Invariant Latitude (Degrees)
70
68
66
64
62
60
58
56
54
07Mar 08Mar 09Mar 10Mar 11Mar 12Mar 13Mar 14Mar 15Mar
Time in 2012 (UT)
Proton cutoff (degrees)
Kp Prediction
Dst Prediction

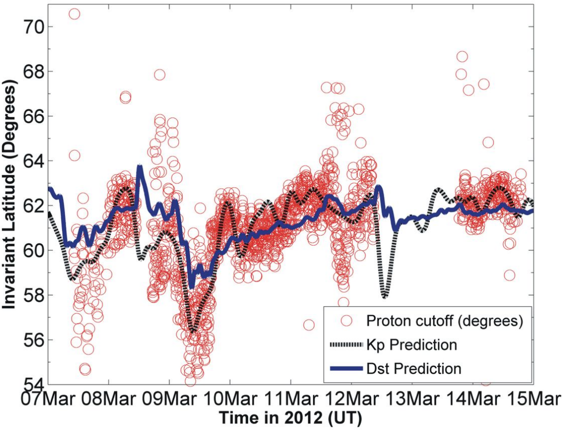
Invariant Latitude (Degrees)
70
68
66
64
62
60
58
56
54
07Mar 08Mar 09Mar 10Mar 11Mar 12Mar 13Mar 14Mar 15Mar
Time in 2012 (UT)
Proton cutoff (degrees)
Kp Prediction
Dst Prediction

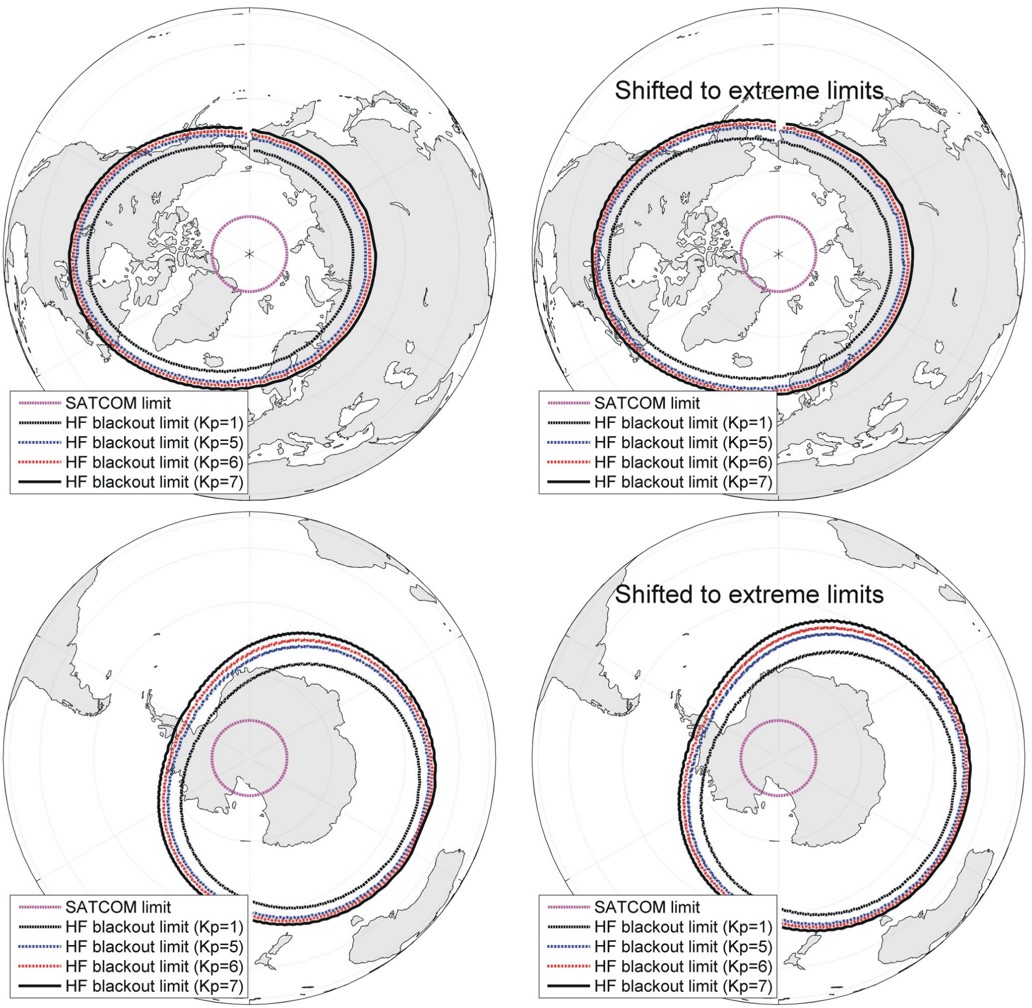

SATCOM limit
HF blackout limit (Kp=1)
HF blackout limit (Kp=5)
HF blackout limit (Kp=6)
HF blackout limit (Kp=7)
Shifted to extreme limits
SATCOM limit
HF blackout limit (Kp=1)
HF blackout limit (Kp=5)
HF blackout limit (Kp=6)
HF blackout limit (Kp=7)
SATCOM limit
HF blackout limit (Kp=1)
HF blackout limit (Kp=5)
HF blackout limit (Kp=6)
HF blackout limit (Kp=7)
Shifted to extreme limits
SATCOM limit
HF blackout limit (Kp=1)
HF blackout limit (Kp=5)
HF blackout limit (Kp=6)
HF blackout limit (Kp=7)